


ORIGINAL RESEARCH

Open Access



Method for co-registration of high-resolution specimen PET-CT with histopathology to improve insight into radiotracer distributions

Luna Maris^{1,2*} , Menekse Göker³, Jens M. Debacker^{4,5,6}, Kathia De Man⁷, Bliede Van den Broeck⁷, Jo Van Dorpe^{8,9}, Koen Van de Vijver^{8,9}, Vincent Keereman^{1,2} and Christian Vanhove^{1,10}

*Correspondence:
luna.maris@ugent.be

¹ Department of Electronics and Information Systems, Medical Image and Signal Processing, Ghent University, Ghent, Belgium

² Clinical Department, XEOS Medical, Ghent, Belgium

³ Department of Gynaecology, Ghent University Hospital, Ghent, Belgium

⁴ Molecular Imaging and Therapy Research Group (MITH), Vrije Universiteit Brussel, Brussels, Belgium

⁵ Department of Nuclear Medicine, UZ Brussel, Brussels, Belgium

⁶ Department of Head and Skin, Head and Neck Surgery Research Group, Ghent University, Ghent, Belgium

⁷ Department of Medical Imaging, Nuclear Medicine, Ghent University Hospital, Ghent, Belgium

⁸ Department of Pathology, Ghent University Hospital, Ghent, Belgium

⁹ Department of Diagnostic Sciences and Cancer Research Institute Ghent (CRIG), Ghent University, Ghent, Belgium

¹⁰ INFINITY Lab, Ghent University, Ghent, Belgium

Abstract

Background: As the spatial resolution of positron emission tomography (PET) scanners improves, understanding of radiotracer distributions in tissues at high resolutions is important. Hence, we propose a method for co-registration of high-resolution ex vivo specimen PET images, combined with computed tomography (CT) images, and the corresponding specimen histopathology.

Methods: We applied our co-registration method to breast cancer (BCa) specimens of patients who were preoperatively injected with 0.8 MBq/kg [¹⁸F]fluorodeoxyglucose ([¹⁸F]FDG). The method has two components. First, we used an image acquisition scheme that minimises and tracks tissue deformation: (1) We acquired sub-millimetre (micro)-PET-CT images of ± 2 mm-thick lamellas of the fresh specimens, enclosed in tissue cassettes. (2) We acquired micro-CT images of the same lamellas after formalin fixation to visualise tissue deformation. (3) We obtained 1 hematoxylin and eosin (H&E) stained histopathology section per lamella of which we captured a digital whole slide image (WSI). Second, we developed an automatic co-registration algorithm to improve the alignment between the micro-PET-CT images and WSIs, guided by the micro-CT of the fixated lamellas. To estimate the spatial co-registration error, we calculated the distance between corresponding microcalcifications in the micro-CTs and WSIs. The co-registered images allowed to study standardised uptake values (SUVs) of different breast tissues, as identified on the WSIs by a pathologist.

Results: We imaged 22 BCa specimens, 13 cases of invasive carcinoma of no special type (NST), 6 of invasive lobular carcinoma (ILC), and 3 of ductal carcinoma in situ (DCIS). While the cassette framework minimised tissue deformation, the best alignment between the micro-PET-CT images and WSIs was achieved after deformable co-registration. We found an overall average co-registration error of 0.74 ± 0.17 mm between the micro-PET images and WSIs. (Pre)malignant tissue (including NST, ILC, and DCIS) generally showed higher SUVs than healthy tissue (including healthy glandular, connective, and adipose tissue). As expected, inflamed tissue and skin also showed high uptake.

Conclusions: We developed a method to co-register micro-PET-CT images of surgical specimens and WSIs with an accuracy comparable to the spatial resolution

of the micro-PET images. While currently, we only applied this method to BCa specimens, we believe this method is applicable to a wide range of specimens and radiotracers, providing insight into distributions of (new) radiotracers in human malignancies at a sub-millimetre resolution.

Keywords: Co-registration method, High-resolution (micro-)PET-CT, Histopathology, Radiotracer distributions, Breast cancer SUVs

Background

Positron emission tomography (PET) and computed tomography (CT) have become widely adopted in oncology [1, 2]. In PET, different types of radiotracers can be used to visualise various tissue characteristics. In order to correctly interpret PET images, we need to understand how radiotracers distribute in different types of tissue. As the correlation of PET images with histopathology is complex, distribution mechanisms are still unclear, even for [¹⁸F]fluorodeoxyglucose ([¹⁸F]FDG), one of the most common radiotracers in oncology [3]. As the spatial resolution of PET scanners is improving, nuclear medicine will soon encounter radiotracer distributions at unprecedented resolutions. Hence, we need to improve our understanding of the distribution of existing and new radiotracers in both cancerous and healthy tissue at high resolutions.

In order to study radiotracer distributions in different tissues, an accurate correlation of PET-CT images with histopathology is required. Published methods perform co-registration between in vivo PET-CT images and histopathology slices of the tissue after surgical resection. Examples are the methods introduced by Schiller et al. [4] and Puri et al. [5, 6] to perform co-registration for the prostate and head and neck region, respectively. Existing methods have several limitations [7]. First, most methods need extensive tissue processing to achieve a match of orientation and cut between PET-CT images and histopathology [7]. For example, Schiller et al. [4] use special embedding and cutting equipment to obtain parallel, contiguously cut, and whole-slice histopathology images of the prostate. This limitation was previously addressed by Puri et al. [5, 6], who developed a method to co-register in vivo PET-CT images of the head and neck region with histopathology slices obtained in routine pathology settings. Second, previously published mathematical co-registration algorithms often rely on minimising the distance between hand-picked pairs of landmarks in the PET-CT and histopathology images [5, 7]. This method is prone to error and sampling bias [8]. Other groups make use of fiducial markers (e.g., laser burns or ink spots) which lead to tissue damage and information loss [5, 9, 10]. Due to these challenges, existing co-registration methods remain time-consuming and labour-intensive, resulting in small patient cohorts [4, 5, 7]. Additionally, almost all publications focus on firm tissues that retain their shape after resection, such as prostate or laryngeal tissue [4, 5, 7]. Correlation is more challenging for soft tissue, such as breast tissue, which is prone to deformation during histopathological processing.

To overcome these challenges, we developed a novel strategy to co-register high-resolution ex vivo PET-CT images with histopathology whole slide images (WSIs). We used a dedicated specimen scanner to capture sub-millimetre (micro-)PET-CT images of resected tissue. Acquiring ex vivo PET-CT images enables maintaining control over tissue deformation, making correlation with histopathology more straightforward. Another advantage of ex vivo tissue scanning is the opportunity to achieve a higher

spatial resolution compared to in vivo scanning, allowing to study radiotracer uptake in tumour and healthy tissue at a sub-millimetre resolution. Several groups already showed that it is feasible to acquire ex vivo (micro-)PET-CT images of oncological specimens in skin [11], breast [12, 13], ovarian [14], prostate [15, 16], head and neck [17, 18], thyroid [19], pancreatic [20], colon [21, 22], liver [22], and lung [23, 24] cancer. While several groups correlated the ex vivo PET-CT imaging results with histopathology, an accurate and systematic approach for co-registration is lacking [12, 15, 17, 18, 21, 23]. In previous work by Debacker et al., we already performed co-registration between autoradiographs of resected human tissue and the corresponding histopathology [17]. However, we did not succeed in directly linking ex vivo micro-PET images with histopathology due to tissue degradation and repositioning caused by the process required to fixate and slice the tissue for histopathological analysis. In this work, we addressed these limitations and developed a co-registration method that minimises, tracks, and compensates for tissue deformation. Our method to accurately align micro-PET-CT images of resected tissue with the corresponding histopathology is inspired by the work of de Boer et al. [8], who performed co-registration of optical measurements of breast tissue with histopathology.

As an example application, we evaluated the proposed co-registration method in breast cancer (BCa). We aligned [^{18}F]FDG micro-PET-CT images of resected BCa specimens with the corresponding histopathology and used the co-registered images to study the standardised uptake values (SUVs) of different types of breast tumours at a sub-millimetre resolution. PET currently has a limited role in BCa diagnosis as its sensitivity depends on the lesion's size and histology [25–28]. It is especially difficult to detect cases of ductal carcinoma in situ (DCIS) and invasive lobular carcinoma (ILC), as these breast tumours generally show lower uptake compared to a case of invasive carcinoma of no special type (NST) [25–28]. By improving our understanding of radiotracer distributions in breast lesions at a sub-millimetre resolution, we get insight into whether improvement in the resolution of PET scanners will enhance the visualisation of BCa in the future.

Methods

Co-registration method

The proposed method consists of two components. First, a strict scheme is followed to acquire micro-PET-CT images of resected oncological specimens, such that, later on, these micro-PET-CT images can easily be correlated with the corresponding histopathology sections. Second, to improve the alignment of both imaging modalities, an automatic mathematical co-registration algorithm is developed and applied.

Image acquisition scheme

We propose an image acquisition scheme to obtain micro-PET-CT images of surgically resected specimens of patients preoperatively injected with a PET radiotracer. This scheme, that minimises and tracks tissue deformation, consists of different steps: (1) After surgical resection, a pathologist slices the obtained specimen into ± 2 mm-thick lamellas. (2) These lamellas are enclosed in standard meshed tissue cassettes. (3) Micro-PET-CT images of the cassettes containing the fresh tissue lamellas are acquired. (4) The tissue is fixated in a buffered formalin solution for at least 12 h. (5) Micro-CT images of the fixated lamellas are acquired to visualise the tissue deformation caused by

the fixation process. (6) The tissue is embedded in paraffin. (7) A $\pm 5 \mu\text{m}$ -thin section is cut from each paraffin block, parallel to the ground plane of the cassette. These tissue sections are mounted on glass slides and coloured using hematoxylin and eosin (H&E) staining. (8) Finally, digital WSIs are obtained from these pathology slides using a slide scanner. All required tissue processing steps are part of the standard-of-care procedure for most tumour specimens. The only adaptation is that the surgical specimen needs to be sliced while it is still fresh, which is not standard practice in all pathologies. Figure 1 visualises this image acquisition scheme in case of a BCa specimen. However, the proposed method can be applied to any surgically resected cancer specimen.

Mathematical co-registration algorithm

While the acquisition scheme minimises tissue deformation, tissue fixation and sectioning will still cause local deformations. To compensate for this, we perform iterative mathematical co-registration of the micro-PET-CT images of the fresh lamellas and the corresponding WSIs. The micro-CT images of the fixated lamellas are used to guide this algorithm. As illustrated in Fig. 2, we apply the following four-step co-registration algorithm:

- I. **Co-register the micro-CTs of the fresh and fixated lamellas** First, we compensate for tissue deformation caused by fixation. We define the transformation that aligns the 3D micro-CT of a fresh lamella (moving image) with the 3D micro-CT of the same lamella after fixation (fixed image). For this step, a free-form B-spline deformation model is used to account for possibly non-uniform deformation due to differences in tissue composition. As tissue densities slightly change during fixation, the normalised correlation coefficient (NCC) is a suited metric to match both micro-CT images.
- II. **Select the micro-CT slice of the fresh lamella that matches the WSI** As a second step, we select one slice of the transformed micro-CT image from step I that

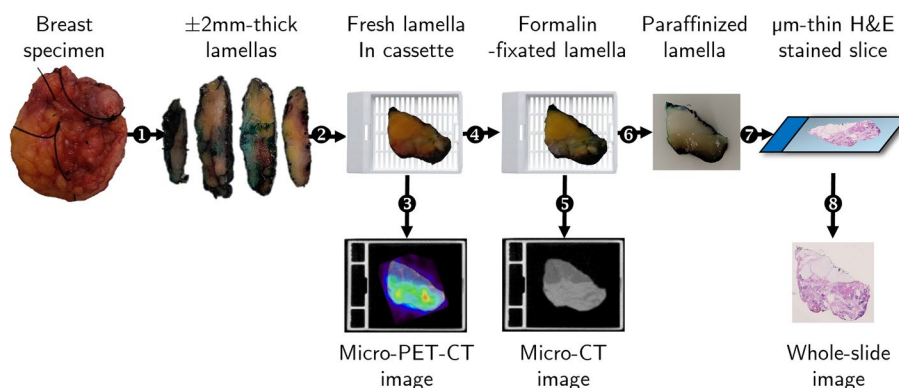


Fig. 1 Illustration of the proposed image acquisition scheme for a breast cancer specimen. (1) Specimen is sliced into $\pm 2 \text{ mm}$ -thick lamellas. (2) Fresh lamellas are enclosed in tissue cassettes and (3) micro-PET-CT images of the fresh tissue are acquired. (4) Lamellas are fixated in formalin and (5) micro-CT images of the fixated tissue are acquired. (6) Lamellas are embedded in paraffin. (7) $\pm 5 \mu\text{m}$ -thin tissue sections are cut, mounted on glass slides, and coloured using a hematoxylin and eosin (H&E) staining, and (8) digital whole slide images (WSIs) are captured from these pathology slides

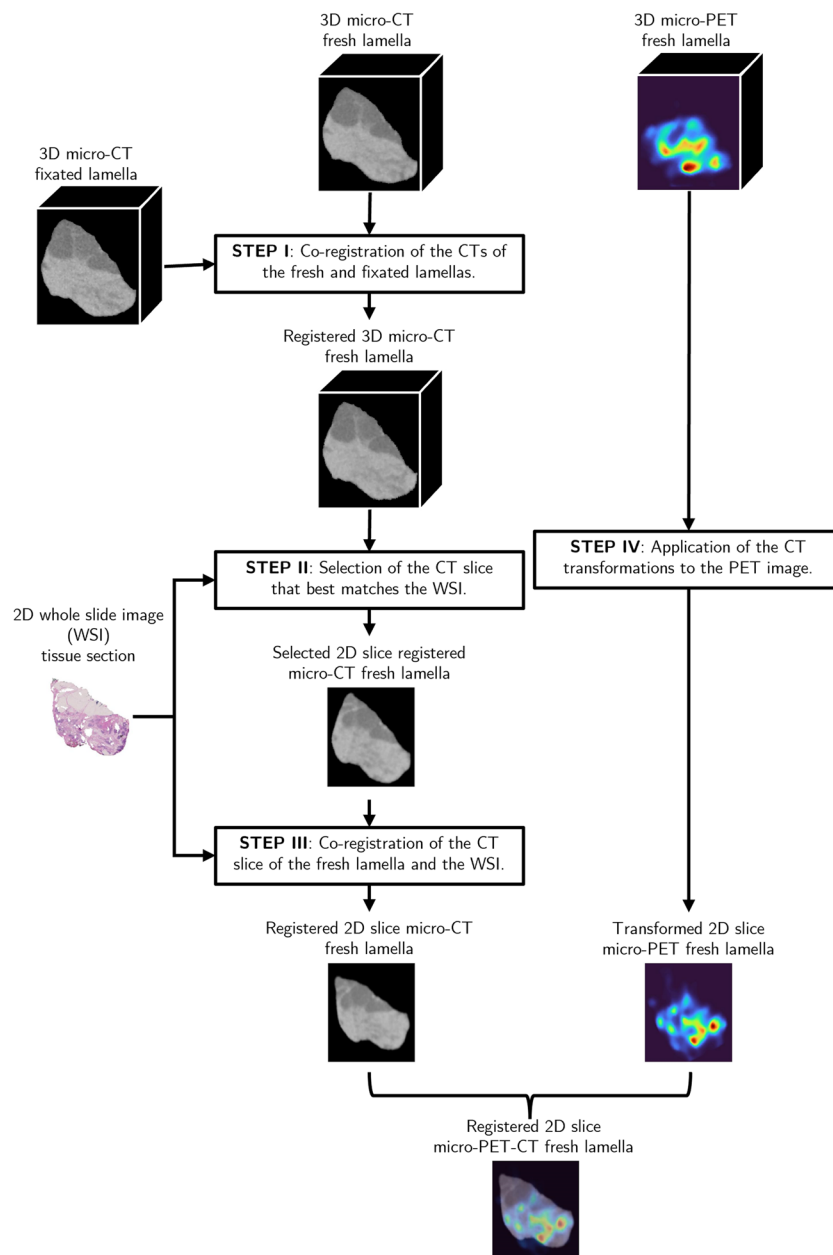


Fig. 2 Illustration of the four-step co-registration algorithm

matches the WSI. The micro-CT is a 3D image of a tissue lamella, while the WSI is a 2D image of a thin section cut from that lamella after paraffin embedding. We match the WSI with a slice of the transformed micro-CT resulting from step I, assuming that most tissue deformation occurs during fixation, not paraffin embedding. We treat the micro-CT as a stack of 2D slices parallel to the cassette surface, with a slice thickness equal to the voxel size of the micro-CT. For every micro-CT slice, we perform an affine co-registration with the WSI, with the normalised mutual information (NMI) as a metric. To express the match of the tissue compositions and shapes in both images, the sum of the NMI and the Sørensen dice simi-

larity coefficient (DSC) is calculated. The micro-CT slice with the highest score after affine co-registration is selected.

- III. **Co-register the selected micro-CT slice and the WSI** As a third step, the selected micro-CT slice (moving image) is co-registered with the WSI (fixed image). As recommended by Albers et al. [29] and de Boer et al. [8], a free-form B-spline deformation is used to compensate for (possibly non-uniform) in-plane deformations caused by sectioning of the paraffin blocks and staining [29]. The NMI metric is again used to match both modalities.
- IV. **Apply the micro-CT transformations to the micro-PET image** Finally, the micro-PET image of the fresh lamella is aligned with the WSI, by applying the transformations found for the corresponding micro-CT image of the fresh lamella. The micro-PET images are not used during the co-registration process, as deforming the PET signal to match the WSI would introduce bias in the PET signal analysis of different tissues.

We used the Python library SimpleElastix [30] to implement this co-registration algorithm. Table 1 lists the key registration components. For every step, we follow a hierarchical multi-resolution strategy to gradually increase data and transformation complexity, making the co-registration more robust. In terms of transformation complexity, we increase the degrees of freedom by sequentially applying a rigid, affine, and (if applicable) B-spline transformation. In terms of data complexity, we apply Gaussian smoothing to the images to create four resolution levels. For every level, 500 co-registration iterations are performed with adaptive stochastic gradient descent (ASGD) as optimiser and linear interpolation.

Application and evaluation in breast cancer

Study design

To demonstrate the feasibility of our co-registration method, we evaluated this technique in BCa. We acquired images of specimens from patients with NST, ILC, or DCIS BCa undergoing breast-conserving surgery at Ghent University Hospital. Patients received a preoperative injection with 0.8 MBq/kg [¹⁸F]FDG. Data collection occurred within two clinical trials (ClinicalTrials.gov identifiers: NCT04343079 and NCT04999917), approved by the local ethics committee. All patients provided written informed consent, agreeing to participation and publication of the results.

Table 1 Registration components for the first three steps of the co-registration algorithm

Component	Step I	Step II	Step III
Moving image	Micro-CT fresh	Registered micro-CT fresh	Selected slice micro-CT fresh
Fixed image	Micro-CT fixated	WSI	WSI
Transformation	Rigid>Affine>B-spline	Rigid>Affine	Rigid>Affine>B-spline
Metric	NCC	NMI	NMI
Optimiser	ASGD	ASGD	ASGD
Interpolator	Linear	Linear	Linear

WSI whole slide image, NCC normalised correlation coefficient, NMI normalised mutual information, ASGD adaptive stochastic gradient descent

Image acquisition

All images were captured following the proposed image acquisition scheme. After the specimen was cut into lamellas, the pathologist visually assessed which lamellas contained macroscopic tumour tissue. From every specimen, one lamella with and one without macroscopic tumour were selected. Large lamellas were further cut to fit the cassettes. Figure 3 provides an overview of all images that were collected for one lamella. The following sections explain in detail how these images were acquired.

Micro-PET-CT imaging of lamellas We acquired micro-PET-CT images of the cassettes containing the fresh lamellas. After fixating the tissue in a 10% neutral buffered formalin solution for 12–18 h, we also acquired micro-CT images of the cassettes with the fixated lamellas. To acquire these micro-PET-CT images, we used a PET-CT specimen imager (AURA 10[®], XEOS Medical NV, Belgium). Only one micro-PET-CT and one micro-CT acquisition per patient was required, as the container of this scanner could simultaneously fit all cassettes. Micro-CT and micro-PET acquisition took 1 min and 10 min respectively. Micro-CT images were reconstructed using filtered back projection (FBP), with an isotropic voxel size of 100 μm. Micro-PET images were reconstructed using 20 iterations of the maximum likelihood expectation maximisation (MLEM) algorithm, with an energy window of 50% around the 511 keV photopeak and an isotropic voxel size of 400 μm. The results were co-registered micro-PET and micro-CT images in DICOM format. The 3D micro-CT images were expressed in Hounsfield units (HUs) and the 3D micro-PET images were converted to lean body mass SUVs using the Janmahasatian formulation [31]. All micro-PET images were attenuation corrected and median filtered (kernel size of 5 × 5 × 5 voxels) to remove noise.

	Fresh breast lamella	Fixated breast lamella	Pathology slide
Optical Photo			
Micro-CT			
Micro-PET-CT			

Fig. 3 Overview of images collected for one breast lamella. (1) Micro-PET-CT image of the fresh lamella, (2) Micro-CT image of the lamella after formalin fixation, and (3) digital whole slide image of the hematoxylin and eosin stained thin tissue section. Only one slice is shown for the 3D micro-PET and micro-CT images. The spatial scale of the images is expressed in mm

Whole slide imaging of H&E stained tissue sections After micro-PET-CT imaging, the cassettes containing the fixated tissue underwent standard clinical processing to obtain one H&E stained tissue section per cassette. Digital WSIs were captured from these sections using a slide scanner (NanoZoomer[®], Hamamatsu Photonics, Japan), resulting in 2D RGB images in NDPI format with a resolution of 0.456 μm .

Mathematical co-registration

Before co-registration, the collected images required preprocessing. We used the resize function from the Python library OpenCV [32] to interpolate the micro-PET images and WSIs to the same isotropic voxel size as the micro-CT images (100 μm). A linear interpolation and an area interpolation were applied to the micro-PET images and WSIs, respectively. Using AMIDE [33], we cropped the micro-PET-CT images to separate the different tissue samples and to remove the cassettes from the micro-CT images. We segmented the tissue in the micro-CT images and WSIs to define binary tissue masks. For the micro-CT images, we applied Otsu's thresholding and selected the largest connected tissue structure using OpenCV. For the WSIs, we manually segmented the largest connected tissue structure using QuPath [34]. The resulting tissue masks were used to remove the background from the micro-CT images and WSIs, and to crop the images with a margin of 5 voxels around the tissue in all directions. Finally, we padded all images that belong to one lamella to the same dimensions, and we converted the WSIs to grey-scale images. After preprocessing the data, the four-step co-registration algorithm was applied.

Co-registration evaluation

The alignment between the transformed micro-PET-CT images of the fresh lamellas and the WSIs was evaluated qualitatively through visual inspection and quantitatively using two different approaches. For the first approach, we calculated the Sørensen DSC, as done by Schiller et al. [4] and de Boer et al. [8]. We calculated the DSC for two types of tissue segmentations: tissue shape, and tissue composition segmentations. For the tissue shape segmentations, we used the binary tissue masks of the micro-CT images and WSIs after co-registration. For the tissue composition segmentations, we distinguished between adipose and non-adipose tissue, as these two tissue types can be separated both in micro-CT images and in WSIs. To separate both tissues in the micro-CT images, we applied Otsu's thresholding to all tissue voxels, after clipping the voxel intensities to [-1000:1000] HUs. The WSIs show the greatest contrast between adipose and non-adipose tissue in the green channel. In QuPath, this channel was manually thresholded after applying the binary tissue mask and a Gaussian filter with a sigma of 1. To calculate the DSC for the composition segmentation, we averaged the DSCs for adipose and non-adipose tissue. The DSC scores based on these tissue shape and composition segmentations are denoted as DSC_{shape} and DSC_{comp} respectively.

As a second evaluation method, we calculated the spatial co-registration error, using an approach similar to Puri et al. [5, 6]. To obtain a mean overall co-registration error between micro-PET and histopathology, we calculated the root sum square (RSS) of the following three co-registration errors:

- (1) Co-registration error between micro-PET and micro-CT of fresh lamellas.

To estimate the misalignment between consecutively acquired micro-PET and micro-CT images, we averaged the co-registration errors of six different micro-PET-CT scanners, measured using an in-house developed calibration phantom.

- (2) Co-registration error between micro-CTs of fresh and fixated lamellas.

To estimate the misalignment between co-registered micro-CTs of the fresh and fixated lamellas (step I), we calculated the distances between pairs of landmarks in both images. As landmarks, we used the microcalcifications that are visible on the micro-CT images. First, we segmented the microcalcifications in the micro-CT images of the fresh lamellas. We thresholded the images at 400 HUs to identify dense structures. The thresholded images were manually corrected to exclude dense spots of marking ink. Next, we identified the corresponding microcalcifications in the micro-CT images of the fixated lamellas following the same approach. Per lamella, we calculated the co-registration error as the root mean square (RMS) of all distances between centres of gravity of corresponding microcalcifications.

- (3) Co-registration error between micro-CT slices of fresh lamellas and WSIs

To estimate the misalignment of co-registered selected micro-CT slices of fresh lamellas and WSIs (step III), we could again employ the microcalcifications as they are also visible on the WSIs. We identified the remaining microcalcifications on the selected micro-CT slices, and a breast pathologist with over 15 years of experience segmented the corresponding microcalcification in the WSIs using QuPath. We selected (clusters of) microcalcifications with a minimal diameter of 100 μm to account for the micro-CT resolution. Per lamella, we again calculated the co-registration error as the RMS of all distances between centres of gravity of corresponding microcalcifications. Note that this method could not address possible mismatches between WSIs and selected micro-CT slices (step II).

Standardised uptake values in breast cancer

The co-registration method establishes a direct mapping between micro-PET-CT images and the corresponding WSIs, facilitating the analysis of radiotracer uptake in different histological tissue types. An experienced breast pathologist annotated the breast WSIs. Using QuPath, (pre)malignant tissue was delineated, distinguishing different histological subtypes: NST, DCIS, and ILC. Other types of benign and healthy tissue that were annotated are lobular carcinoma in situ (LCIS), hyperplasia, inflamed tissue, healthy glands, and skin. The remaining tissue was separated into adipose and connective tissue, using a threshold as described above.

We used these annotations together with the co-registered micro-PET images to calculate the mean and maximum SUVs (SUV_{mean} and SUV_{max}) of different breast tissues. In order to do this, we assigned one tissue label to every PET pixel. The WSI annotations were exported with an isotropic pixel size of 3.6 μm . To interpolate these

annotations to the 100 μm pixel size of the micro-PET images, we used a method that accounts for the spatial resolution of micro-PET. The signal of a PET pixel can be seen as a weighted sum of signals originating from different tissues surrounding the PET pixel. The relative contribution of a tissue signal to the PET pixel signal decreases with distance from the PET pixel. These relative contribution weights can be represented by a normalised 2D Gaussian kernel that is centred on the PET pixel. In correspondence with the resolution of the micro-PET scanner, we use a Gaussian kernel with a full width at half maximum (FWHM) of 1 mm and a size ranging from -3σ to $+3\sigma$ in both directions. To every PET pixel, we assign the label of the tissue type that has the highest total relative weight, and as such contributes the most to the PET pixel signal. In practice, this can be seen as a filtering process. The Gaussian kernel is scanned over the full resolution annotation with a stride of 100 μm in both directions. At every kernel position, corresponding to one PET pixel, we select the tissue type with the highest total relative weight according to the Gaussian kernel. This filtering process is illustrated in Fig. 4.

Results

Study subjects

We acquired images of BCa specimens from 22 patients. Specimens included 13 NST, 6 ILC, and 3 DCIS cases. In total, we imaged 33, 16, and 10 cassettes of NST, ILC, and DCIS specimens respectively.

Image acquisition in breast cancer

Micro-PET-CT imaging of the fresh breast lamellas was successful in all cases. The mean time between ^{18}F FDG injection and micro-PET acquisition was $4\text{h}31\text{min} \pm 48\text{min}$ across all patients. After formalin fixation, micro-CT images of all lamellas could be captured. Comparing the 3D binary tissue masks of the micro-CT images before and after

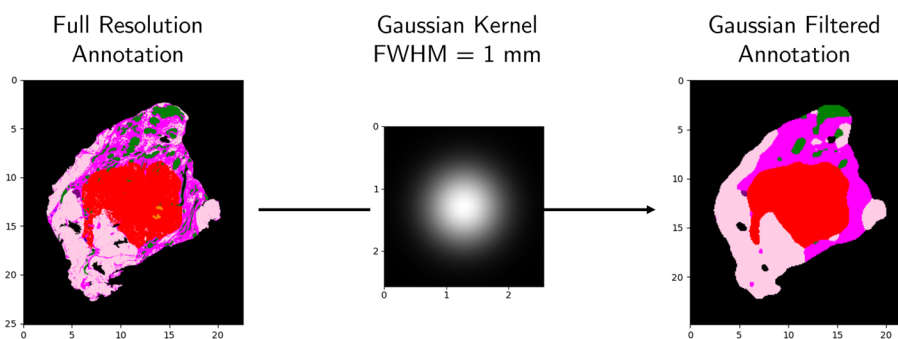


Fig. 4 Illustration of the Gaussian filtering process of a tissue annotation. The figure illustrates how a full resolution annotation with an isotropic pixel size of 3.6 μm is turned into a Gaussian filtered annotation with an isotropic pixel size of 100 μm . The Gaussian kernel with full width at half maximum (FWHM) of 1 mm is scanned over the original annotation with a stride of 100 μm , and at every position the label of the tissue type with the highest relative weight is chosen. The spatial scale of the images is expressed in mm. Note that the Gaussian kernel is not displayed in its actual relative size

fixation revealed an average tissue volume increase of $0.2 \pm 4.3\%$ relative to the volume of the fresh lamellas across all patients. Thus, some lamellas slightly increased in volume, while others slightly decreased. We did not observe any relation between tissue volume increase during fixation and tissue composition in terms of the volume ratio of adipose and non-adipose tissue in a lamella. We have to keep in mind that these results might be affected by partial volume effects in the micro-CT images.

On average, it took 3 days from the moment where the specimen arrived at the pathology lab, to obtain the H&E stained pathology slides. WSIs of the pathology slides could be acquired for all lamellas. A clear correlation between the micro-PET-CT images and histopathology was immediately visible, due to the cassette framework that minimised tissue deformation.

Mathematical co-registration in breast cancer

Mathematical co-registration of the micro-CT images of the fresh lamellas with the WSIs was performed fully automatically (after preprocessing). The entire co-registration pipeline took on average 5 ± 2 min across all lamellas when run on an 11th Gen Intel Core i7 CPU. The intermediate results of the co-registration process are visualised for one lamella in Fig. 5. Table 2 displays quantitative metrics to show the improvement in image alignment after the different co-registration steps.

The found transformations were applied to the micro-PET images of the fresh lamellas. Figure 6 shows the resulting alignment of the micro-PET-CT images of the fresh lamellas and the corresponding WSIs for some representative NST, ILC, and DCIS cases. The mathematical co-registration further optimised the alignment between the micro-PET-CT images and WSIs, showing a good correspondence between both imaging modalities in all cases.

To estimate the mean overall co-registration error between micro-PET and histopathology, we calculated the RSS of three co-registration errors. The mean co-registration error between the micro-PET and micro-CT images of the fresh lamellas was 0.35 ± 0.06 mm. In the micro-CT images of the fresh lamellas, we identified 25 microcalcifications across 11 lamellas of 11 patients. Corresponding microcalcifications were easily identified in the micro-CT images of the fixated lamellas. After co-registering the micro-CTs of the fresh and fixated lamellas (step I), the mean co-registration error was 0.25 ± 0.28 mm across the 11 lamellas. After selecting micro-CT slices matching the WSIs (step II), 7 microcalcifications across 5 slices remained. All corresponding microcalcifications were found in the WSIs. After co-registering the micro-CT slices and WSIs (step III), the mean co-registration error was 0.60 ± 0.22 mm across the 5 slices. The resulting RSS of these three errors was 0.74 ± 0.17 mm, averaged across the 5 lamella slices for which all three errors could be calculated. Figure 7 visualises the centres of gravity of corresponding microcalcifications in the micro-CT images and WSIs for one lamella.

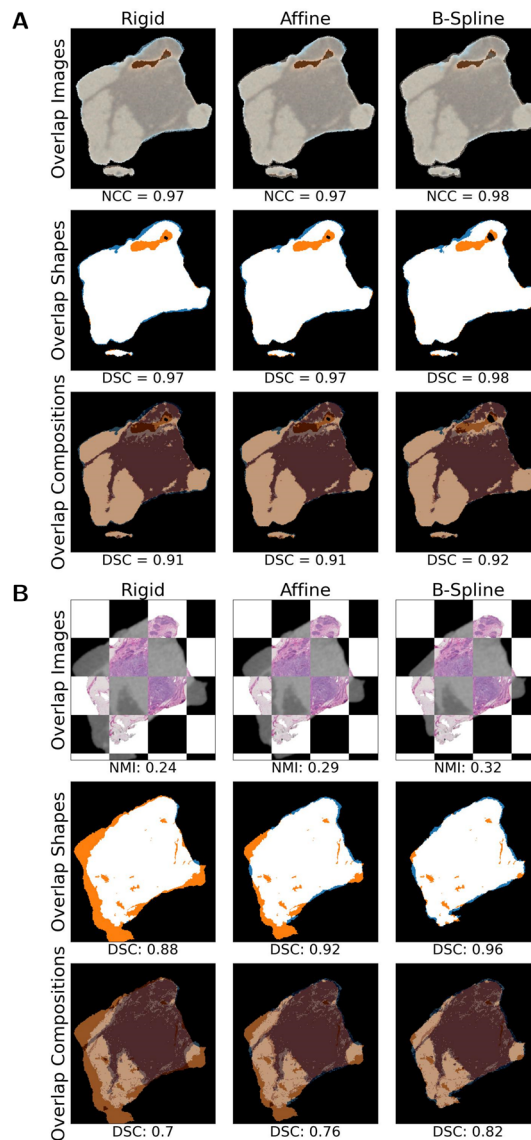


Fig. 5 Intermediate results of the mathematical co-registration process for one breast lamella. **A** Alignment between the CTs of the fresh and fixated lamella after rigid, affine and B-spline co-registration. Colour fusions show the overlap between both micro-CT images, as well as their shape and composition segmentations. The overlap metrics (normalised correlation coefficient (NCC) and dice similarity coefficient (DSC)) are shown below the images. Only a central slice of the 3D micro-CT images is shown. **B** Alignment of the selected micro-CT slice of the fresh lamella with the histopathology whole slide image (WSI) after rigid, affine and B-spline co-registration. Chequerboards show the overlap between the micro-CT image and WSI, and colour fusions show the overlap between their shape and composition segmentations. The overlap metrics (normalised mutual information (NMI) and DSC) are shown below the images

Standardised uptake values in breast cancer

After co-registration, we used the annotations to calculate the SUVs of different breast tissues. Examples of these annotations are shown in Fig. 6, together with the aligned micro-PET-CT images. Table 3 shows the average and standard deviation of SUV_{mean} and SUV_{max} per breast tissue type, as defined by the Gaussian filtered annotations. The average and standard deviation are calculated across the patients. The

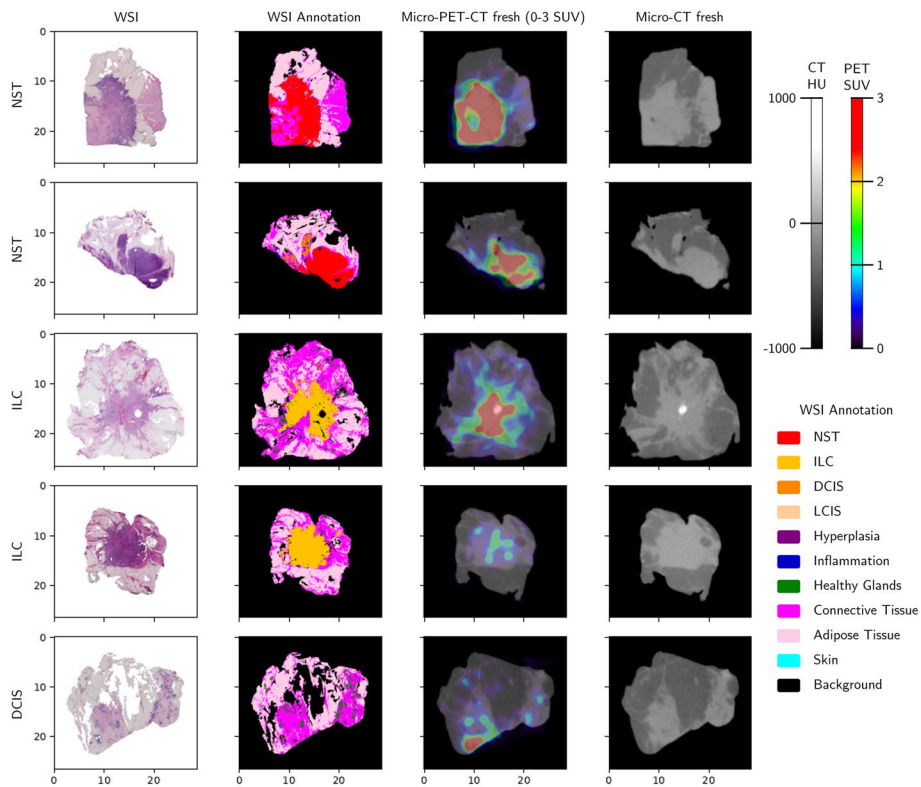


Fig. 6 Overview of the alignment between the micro-PET-CT images and histopathology whole slide images (WSIs) after mathematical co-registration. Representative lamellas containing different breast tumours are shown: 2 carcinomas of no special type (NST), 2 invasive lobular carcinomas (ILCs), and 1 ductal carcinoma in situ (DCIS). For each lamella the following images are shown: the WSI, the WSI annotation, the co-registered micro-PET-CT image of the fresh lamella, and the micro-CT image without the micro-PET overlay. The original unfiltered WSI annotations are shown. Micro-PET images are displayed with an absolute window of 0-3 standardised uptake values (SUVs) and micro-CT images are shown in Hounsfield units (HUs). The spatial scale of the images is expressed in mm

Table 2 Quantitative metrics expressing the image alignment after the different co-registration steps

	NCC	NMI	DSC _{shape}	DSC _{comp}
Co-registration of the CTs of the fresh and fixated lamella				
Unaligned	0.87 ± 0.07	–	0.88 ± 0.06	0.71 ± 0.11
Rigid	0.93 ± 0.05	–	0.93 ± 0.04	0.79 ± 0.09
Affine	0.94 ± 0.03	–	0.95 ± 0.03	0.81 ± 0.08
B-spline	0.96 ± 0.01	–	0.97 ± 0.01	0.84 ± 0.06
Co-registration of the micro-CT slice of the fresh lamella and the WSI				
Unaligned	–	0.18 ± 0.05	0.79 ± 0.11	0.52 ± 0.14
Rigid	–	0.20 ± 0.05	0.82 ± 0.11	0.56 ± 0.15
Affine	–	0.24 ± 0.04	0.88 ± 0.07	0.62 ± 0.13
B-spline	–	0.27 ± 0.04	0.91 ± 0.07	0.65 ± 0.14

The mean ± standard deviation of all quantitative metrics across the different lamellas are shown after every co-registration step. WSI whole slide image, NCC normalised correlation coefficient, NMI normalised mutual information, DSC dice similarity coefficient

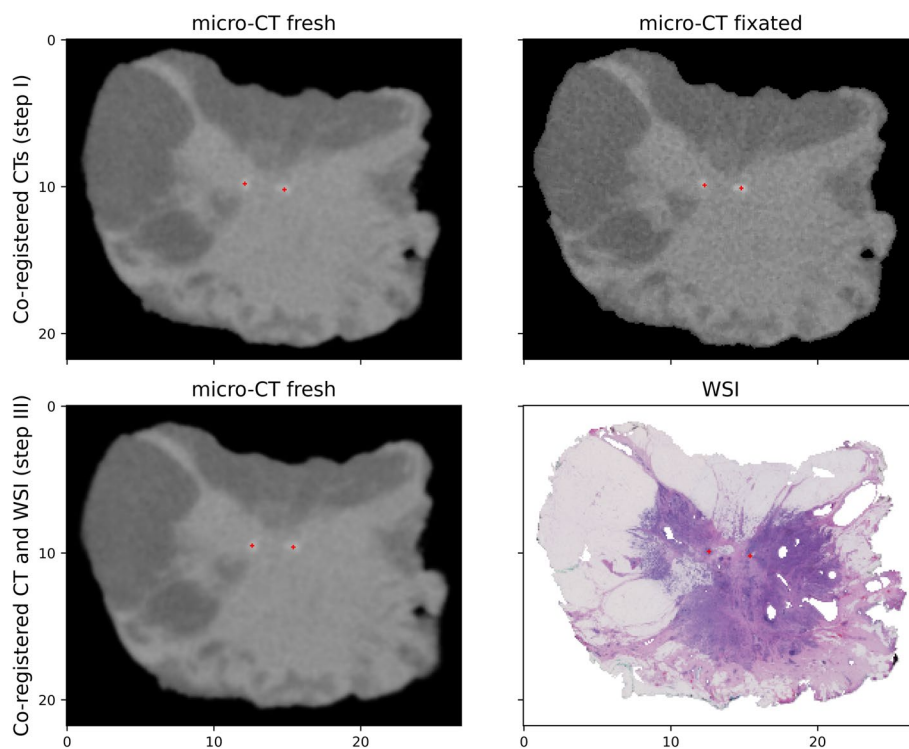


Fig. 7 Illustration of corresponding microcalcifications in micro-CT images and histopathology whole slide images (WSIs). The top row shows one slice of the aligned micro-CTs of the fresh and fixated lamellas after co-registration step I. The bottom row shows the aligned micro-CT slice and WSI after co-registration step III. Red crosses indicate the centres of gravity of 2 microcalcifications in all images. The spatial scale of the images is expressed in mm

box plots in Fig. 8 give a more detailed view on the spread in SUV_{mean} and SUV_{max} across all patients.

Discussion

We developed a method for co-registration of sub-millimetre PET images of ex vivo tissue lamellas with the corresponding histopathology. While the idea of imaging sliced tissue specimens as an intermediate co-registration step was already introduced by Puri et al. [6], our method has several advantages over existing co-registration methods that align in vivo PET images with histopathology [4, 5, 7–10]. First, the only requirement of our method, in addition to the standard histopathological processing, is that the tissue should be sliced in lamellas while it is still fresh. Second, our mathematical co-registration method is fully automatic as we use intensity-based similarity metrics based on the entire images. Finally, ex vivo PET imaging of tissue allows visualising radiotracer uptake at a sub-millimetre resolution that cannot yet be reached by in vivo PET scanners.

We applied the proposed method to resected BCa specimens. The micro-PET-CT images and the corresponding WSIs showed good visual alignment after co-registration. Quantitative metrics (NCC, NMI, and DSC scores) improved with more complex co-registration transformations. This indicates the need to correct for free-from deformations to reach accurate alignment, consistent with the conclusions of de Boer

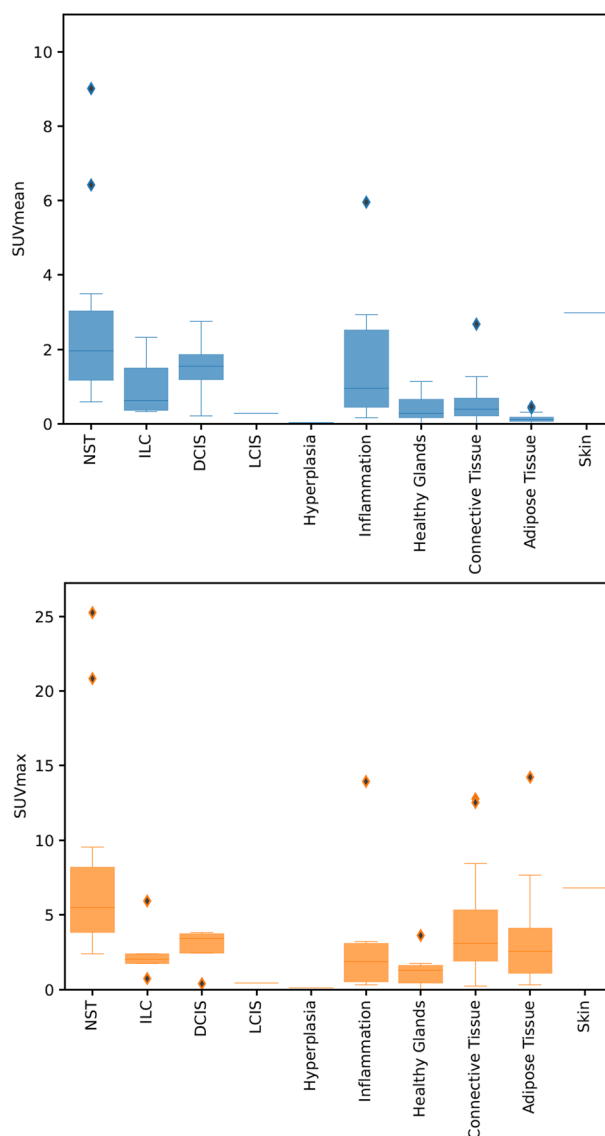


Fig. 8 Box plots showing the spread in standardised uptake values (SUVs) of different breast tissues. The top plot shows the spread in SUV_{mean} , while the bottom plot shows the spread in SUV_{max} across all patients

et al. [8]. Schiller et al. [4] reported a maximal DSC of 0.90 ± 0.02 for the overlap between the prostate shapes in in vivo CT and histopathology. A maximal DSC of 0.94 ± 0.02 was reported by de Boer et al. [8] for the overlap between the breast tissue shapes in ex vivo white light images and histopathology. While not strictly comparable, we found a similar maximal DSC of 0.91 ± 0.07 for the overlap between the breast tissue shapes in ex vivo micro-CT slices of the fresh lamellas and WSIs. The DSC_{comp} scores were lower than the DSC_{shape} scores. This is most likely influenced by the fact that CT images do not always show high contrast between adipose and non-adipose tissue, resulting in small inaccuracies in the composition segmentations. Using the microcalcifications as landmarks, we found a mean overall co-registration error between micro-PET and histopathology of 0.74 ± 0.17 mm, which is

Table 3 Standardised uptake values (SUVs) of different breast tissues as measured in [¹⁸F]FDG micro-PET images

	SUV _{mean}	SUV _{max}
NST	2.70 ± 2.38	7.85 ± 6.81
ILC	1.02 ± 0.87	2.57 ± 1.98
DCIS	1.51 ± 1.04	2.77 ± 1.61
LCIS	0.28	0.43
Hyperplasia	0.04	0.09
Inflammation	1.89 ± 2.23	3.59 ± 5.22
Healthy glands	0.44 ± 0.44	1.30 ± 1.22
Connective tissue	0.56 ± 0.59	4.19 ± 3.49
Adipose tissue	0.15 ± 0.12	3.38 ± 3.22
Skin	2.99	6.80

The mean ± standard deviation of SUV_{mean} and SUV_{max} across all patients are shown. NST carcinoma of no special type, ILC invasive lobular carcinoma, DCIS ductal carcinoma in situ, LCIS lobular carcinoma in situ

comparable to the spatial resolution of the used specimen micro-PET scanner. This error is also smaller than the co-registration error of 3.0 ± 0.7 mm reported by Puri et al. [5, 6] for the alignment between in vivo PET images and histopathology slices in laryngeal cancer. These results show that the proposed co-registration method is successful, even for soft tissue like breast tissue.

There are many possible applications of the proposed co-registration method. We showed that in case of BCa, this technique can be used to study the uptake of [¹⁸F]FDG in different types of breast tissue at a high resolution. According to the resulting SUV_{mean} values, (pre)malignant tissue (including NST, ILC, and DCIS) in general showed higher uptake compared to healthy tissue (including healthy glandular, connective, and adipose tissue). ILC and DCIS showed lower uptake compared to NST, which corresponds to what is reported in literature for in vivo [¹⁸F]FDG PET [25, 27, 28, 35, 36]. While it is often difficult to detect ILC and DCIS in in vivo PET, our results suggest that micro-PET-CT images can visualise ILC and DCIS tumours. LCIS and hyperplasia showed low uptake, in the same range as healthy tissue. As expected, we also found notable uptake of [¹⁸F]FDG in inflamed tissue and in the skin. It is known that [¹⁸F]FDG suffers from low specificity and can show non-specific uptake in inflamed tissue, in benign hyperplasia, in sebaceous glands in the skin, and even in healthy breast glands [25, 27, 35].

In terms of SUV_{max} values, our results were generally higher compared to values reported by other groups in case of in vivo [¹⁸F]FDG PET. Fujii et al. found mean SUV_{max} values of 3.44 ± 3.03 and 2.25 ± 1.99 for NST and ILC respectively [28]. Azuma et al. found a mean SUV_{max} of 2.9 ± 0.5 for the DCIS subtype [36]. Uptake of normal breast tissue is in general found to be homogeneous, with SUV_{max} below 2.5 [35, 37]. The specimen SUV_{max} values that we found follow the same trend, but are in general higher. A possible reason for this is that the improved spatial resolution of ex vivo PET reduces the partial volume effect [38]. In addition, specimen PET does not suffer from decreased SUVs caused by respiratory motion [38].

We found a wide range of BCa SUVs. In addition to the histological BCa type, there are other factors that influence tumour SUVs. For example, the molecular subtype and grade of the tumour also influence [¹⁸F]FDG uptake, as well as the tumour cell density,

the microvessel density, and the level of tumour infiltrating immune cells [25, 27, 28, 35, 36, 39–41]. In future work, we will further investigate the relation between breast tumour characteristics and radiotracer uptake.

The proposed co-registration method bridges the gap between high-resolution molecular imaging and histopathology, stimulating the novel field of transpathology as introduced by Tian et al. [42]. The method provides a unique opportunity to study the distribution of existing and new radiotracers in different types of human tissue at a sub-millimetre resolution. These insights will help nuclear medicine physicians to correctly interpret clinical PET scans, in particular when the resolution of PET scanners improves. The co-registered micro-PET-CT images and WSIs also allow gaining more insight into the tumour microenvironment and the underlying causes of heterogeneity in tumour metabolism, which we will further investigate in future work. These findings may eventually result in more personalised patient care.

While the co-registration method shows good results, there are some limitations. First, the micro-CT images and the corresponding WSIs can never be matched perfectly due to artefacts in the WSIs. During sectioning and colouring of the tissue sections, tissue folds and tears can occur, and small tissue pieces can break off [43]. These artefacts can lead to strong local deformations in the micro-CT images during co-registration. Second, the limited soft tissue contrast of the CT images limits the co-registration accuracy. Third, in the proposed method we make the assumption that the tissue section in the WSI can be matched with a section of the fixated lamella, parallel to the cassette surface. This is an approximation as the tissue might slightly deform when embedding it in paraffin. In addition, cutting may not be performed perfectly parallel to the cassette surface.

Furthermore, the strategy we used to evaluate the spatial co-registration error based on pairs of microcalcifications, also has several shortcomings. First, this evaluation method is not entirely independent as we used intensity-based metrics to perform fully automatic co-registration. Second, not all imaged tissue lamellas contained microcalcifications, so we could only estimate the co-registration error for a subset of the data. Third, large microcalcifications can migrate or even get lost during preparation of the histopathology slides, possibly affecting the co-registration error.

Finally, the approach we used to calculate breast tissue SUVs also has some limitations. First, as we are comparing a micro-PET image with an isotropic resolution of around 1 mm with a histopathology WSI with a resolution of 0.456 μm and a thickness of around 5 mm, partial volume effects inevitably influence the results. While we perform 2D Gaussian filtering of the WSI annotations to account for the limited in-plane micro-PET resolution, the PET signal is influenced by the 3D tissue configuration. These partial volume effects will lead to partial volume loss, as well as spillover, which may explain why the resulting SUV_{max} values of healthy glandular, connective, and adipose tissue are rather high. As mentioned by Puri et al. [6], obtaining contiguous histopathology slices to account for the 3D tissue configuration would be more accurate, but introduces unwanted complexity in the co-registration strategy. Second, there are also limitations to the accuracy of the annotations. For maximal accuracy, the annotations should be performed on cellular level, which is not feasible to do manually. Third, the time between radiotracer injection and imaging was quite

large, which might have increased the image noise levels. However, in general, visual inspection of the images showed clear PET signals.

Conclusion

We developed a novel method to accurately and automatically co-register high-resolution PET-CT images with histopathology in resected tissue. Our method consists of an image acquisition scheme that minimises and tracks tissue deformation, followed by a mathematical co-registration algorithm to further optimise image alignment. Our method is less labour-intensive and time-consuming compared to previously proposed protocols, making it feasible to study larger patient groups.

We applied our method to BCa specimens and showed that, even for highly deformable breast tissue, co-registration can be successfully performed with an accuracy comparable to the spatial resolution of micro-PET. We collected a unique dataset of [^{18}F]FDG micro-PET-CT images of breast tissue that are co-registered with the corresponding histopathology. This allowed a detailed study of SUVs of different types of breast tissue. We found that (pre)malignant breast tissue in general shows higher uptake compared to healthy tissue. This not only includes the NST tumours, but also the ILC and DCIS subtypes that are in general more difficult to detect in *in vivo* PET. As expected, high non-specific uptake was also detected in inflamed tissue and in the skin.

We believe that the proposed technique can also be applied to other types of tumours and radiotracers. The proposed method can provide a better understanding of the *in vivo* distribution of (new) radiotracers in different tissues on a sub-millimetre scale, and may clarify the underlying mechanisms of radiotracer uptake. These insights will eventually improve clinical practice and patient care.

Acknowledgements

The authors would like to express their gratitude to Leen Van de Sande and Anneleen Kiekens for the assistance with the data collection.

Author contributions

LM developed the co-registration method and implemented the mathematical co-registration algorithm with the support of VK, CV, and JD. LM acquired the imaging data for this manuscript together with MG, who performed the breast-conserving surgeries, and KDM and BVdB, who performed the preoperative radiotracer injections. KVdV annotated all histopathology WSIs. LM analysed and interpreted the results with the support of VK, CV, and KVdV. LM wrote the manuscript, and all authors commented on the manuscript. All authors read and approved the final manuscript.

Funding

This project has received funding from VLAIO through a Baekeland mandate with project ID HBC.2022.0175.

Availability of data and materials

The datasets generated and analysed during the current study are not publicly available, but are available from the corresponding author on reasonable request.

Declarations

Ethics approval and consent to participate

All data for this manuscript were collected at the Ghent University Hospital (Belgium) in the context of two clinical trials (ClinicalTrials.gov identifiers: NCT04343079 and NCT04999917), approved by the ethics committee affiliated with the Ghent University Hospital. All patients provided written informed consent, agreeing to participation in the study and publication of the results.

Consent for publication

All patients participating in the study provided written informed consent, agreeing to participation in the study and publication of the results.

Competing interests

LM is a research engineer at XEOS Medical, and VK is a shareholder and board member of XEOS Medical. MG, JD, KDM, BVdB, JVD, KVdV, and CV declare that they have no conflict of interest.

Received: 11 March 2024 Accepted: 4 September 2024

Published online: 14 October 2024

References

1. Ul-Hassan F, Cook GJ. PET/CT in oncology. *Clin Med*. 2012;12(4):368–72.
2. Paydary K, Seraj SM, Zadeh MZ, Emamzadehfard S, Shamchi SP, Gholami S, et al. The evolving role of FDG-PET/CT in the diagnosis, staging, and treatment of breast cancer. *Mol Imag Biol*. 2019;21(1):1–10.
3. Meyer HJ, Wienke A, Surov A. Associations between GLUT expression and SUV values derived from FDG-PET in different tumors—a systematic review and meta analysis. *PLoS ONE*. 2019;14(6): e0217781.
4. Schiller F, Fechter T, Zamboglou C, Chirindel A, Salman N, Jilg CA, et al. Comparison of PET/CT and whole-mount histopathology sections of the human prostate: a new strategy for voxel-wise evaluation. *EJNMMI Phys*. 2017;4(1):21.
5. Puri T, Chalkidou A, Henley-Smith R, Roy A, Barber PR, Guerrero-Urbano T, et al. A method for accurate spatial registration of PET images and histopathology slices. *EJNMMI Res*. 2015;5(1):64.
6. Puri T, Chalkidou A, Roy A, Henley-Smith R, Barber PR, Oakley R, et al. A method for accurate spatial registration of PET images and histopathology slices. *Oncol News*. 2016;11:10–2.
7. Sen A, Troncoso P, Venkatesan A, Pagel MD, Nijkamp JA, He Y, et al. Correlation of in-vivo imaging with histopathology: a review. *Eur J Radiol*. 2021;144: 109964.
8. de Boer LL, Kho E, Nijkamp J, Vijver KKV, Sterenberg HJCM, Beek LCT, et al. Method for coregistration of optical measurements of breast tissue with histopathology: the importance of accounting for tissue deformations. *J Biomed Opt*. 2019;24(7): 075002.
9. Unger J, Sun T, Chen YL, Phipps JE, Bold RJ, Darrow MA, et al. Method for accurate registration of tissue autofluorescence imaging data with corresponding histology: a means for enhanced tumor margin assessment. *J Biomed Opt*. 2018;23(1): 015001.
10. Laughney AM, Krishnaswamy V, Rizzo EJ, Schwab MC, Barth RJ, Pogue BW, et al. Scatter spectroscopic imaging distinguishes between breast pathologies in tissues relevant to surgical margin assessment. *Clin Cancer Res Off J Am Assoc Cancer Res*. 2012;18(22):6315–25.
11. Povoski SP, Hall NC, Martin EW, Walker MJ. Multimodality approach of perioperative 18F-FDG PET/CT imaging, intraoperative 18F-FDG handheld gamma probe detection, and intraoperative ultrasound for tumor localization and verification of resection of all sites of hypermetabolic activity in a case of occult recurrent metastatic melanoma. *World J Surg Oncol*. 2008;6(1):6.
12. Göker M, Marcinkowski R, Van Bockstal M, Keereman V, Van Holen R, Van Dorpe J, et al. 18F-FDG micro-PET/CT for intra-operative margin assessment during breast-conserving surgery. *Acta Chir Belg*. 2020;120(5):366–74.
13. Hall NC, Povoski SP, Murrey DA, Knopp MV, Martin EW. Combined approach of perioperative 18F-FDG PET/CT imaging and intraoperative 18F-FDG handheld gamma probe detection for tumor localization and verification of complete tumor resection in breast cancer. *World J Surg Oncol*. 2007;5(1):143.
14. Cohn DE, Hall NC, Povoski SP, Seamon LG, Farrar WB, Martin EW. Novel perioperative imaging with 18F-FDG PET/CT and intraoperative 18F-FDG detection using a handheld gamma probe in recurrent ovarian cancer. *Gynecol Oncol*. 2008;110(2):152–7.
15. Muraglia L, Mattana F, Travaini LL, Musi G, Bertani E, Renne G, et al. First live-experience session with PET/CT specimen imager: a pilot analysis in prostate cancer and neuroendocrine tumor. *Biomedicines*. 2023;11(2):645.
16. Darr C, Costa PF, Kahl T, Moraitis A, Engel J, Al-Nader M, et al. Intraoperative molecular positron emission tomography imaging for intraoperative assessment of radical prostatectomy specimens. *Eur Urol Open Sci*. 2023;54:28–32.
17. Debacker JM, Schelfhout V, Brochez L, Creytens D, D'Asseler Y, Deron P, et al. High-resolution 18F-FDG PET/CT for assessing three-dimensional intraoperative margins status in malignancies of the head and neck, a proof-of-concept. *J Clin Med*. 2021;10(16):3737.
18. Debacker JM, Maris L, Cordier F, Creytens D, Deron P, Descamps B, et al. Direct co-registration of [18F]FDG uptake and histopathology in surgically excised malignancies of the head and neck: a feasibility study. *Eur J Nucl Med Mol Imag*. 2023;50(7):2127–39.
19. Agrawal A, Hall NC, Ringel MD, Povoski SP, Martin EW. Combined use of perioperative TSH-stimulated 18F-FDG PET/CT imaging and gamma probe radio guided surgery to localize and verify resection of iodine scan-negative recurrent thyroid carcinoma. *Laryngosc*. 2008;118(12):2190–4.
20. Maris L, De Man K, Gryspeerdt F, Hoorens A, Keereman V, Kiekens A, et al. Abstract: 18F-FDG-PET-CT specimen imaging for perioperative visualization of pancreatic adenocarcinoma: a proof-of-concept study. ESSO41 - Online Congress Portal - Presentation number: P292; 2022.
21. Gollub MJ, Akhurst TJ, Williamson MJ, Shia J, Humm JL, Wong WD, et al. Feasibility of ex vivo FDG PET of the colon. *Radiology*. 2009;252(1):232–9. <https://doi.org/10.1148/radiol.2522081864>.
22. Hall NC, Povoski SP, Murrey DA, Knopp MV, Martin EW. Bringing advanced medical imaging into the operative arena could revolutionize the surgical care of cancer patients. *Expert Rev Med Dev*. 2008;5(6):663–7. <https://doi.org/10.1586/17434440.5.6.663>.
23. Van Baardwijk A, Bosmans G, Van Suylen RJ, Van Kroonenburgh M, Hochstenbag M, Geskes G, et al. Correlation of intra-tumour heterogeneity on 18F-FDG PET with pathologic features in non-small cell lung cancer: a feasibility study. *Radiother Oncol*. 2008;87(1):55–8.
24. Moffatt-Bruce SD, Povoski SP, Sharif S, Hall NC, Ross P, Johnson MA, et al. A novel approach to positron emission tomography in lung cancer. *Ann Thoracic Surg*. 2008;86(4):1355–7.
25. Hadebe B, Harry L, Ebrahim T, Pillay V, Vorster M. The role of PET/CT in breast cancer. *Diagnostics*. 2023;13(4):597.
26. Yang SK, Cho N, Moon WK. The role of PET/CT for evaluating breast cancer. *Korean J Radiol*. 2007;8(5):429–37.
27. Ulaner GA. PET/CT for patients with breast cancer: Where is the clinical impact? *AJR Am J Roentgenol*. 2019;213(2):254–65.

28. Fujii T, Yajima R, Kurozumi S, Higuchi T, Obayashi S, Tokiniwa H, et al. Clinical significance of 18F-FDG-PET in invasive lobular carcinoma. *Anticancer Res.* 2016;36(10):5481–5.
29. Albers J, Svetiove A, Alves J, Kraupner A, di Lillo F, Markus MA, et al. Elastic transformation of histological slices allows precise co-registration with microCT data sets for a refined virtual histology approach. *Sci Rep.* 2021;11(1):10846.
30. Marstal K, Berendsen F, Staring M, Klein S. SimpleElastix: A User-Friendly, Multi-lingual Library for Medical Image Registration. 2016 IEEE Conference on Computer Vision and Pattern Recognition Workshops (CVPRW). 2016;p. 574–582. Conference Name: 2016 IEEE Conference on Computer Vision and Pattern Recognition Workshops (CVPRW) ISBN: 9781509014378 Place: Las Vegas, NV, USA Publisher: IEEE.
31. Janmahasatian S, Duffull SB, Ash S, Ward LC, Byrne NM, Green B. Quantification of lean bodyweight. *Clin Pharmacokinet.* 2005;44(10):1051–65.
32. Itseez. Open Source Computer Vision Library; 2015. Available from: <https://github.com/itseez/opencv>.
33. Loening A, Gambhir S. AMIDE: a free software tool for multimodality medical image analysis. *Mol Imaging*; 2003; 2.
34. Bankhead P, Loughrey MB, Fernández JA, Dombrowski Y, McArt DG, Dunne PD, et al. QuPath: open source software for digital pathology image analysis. *Sci Rep.* 2017;7(1):16878.
35. Dong A, Wang Y, Lu J, Zuo C. Spectrum of the breast lesions with increased 18F-FDG uptake on PET/CT. *Clin Nucl Med.* 2016;41(7):543–57.
36. Azuma A, Tozaki M, Ito K, Fukuma E, Tanaka T, O'uchi T. Ductal carcinoma in situ: correlation between FDG-PET/CT and histopathology. *Radiat Med.* 2008;26(8):488–93.
37. Zytoon AA, Murakami K, El-Kholy MR, El-Shorbagy E, Ebied O. Breast cancer with low FDG uptake: characterization by means of dual-time point FDG-PET/CT. *Eur J Radiol.* 2009;70(3):530–8.
38. Kinahan PE, Fletcher JW. PET/CT standardized uptake values (SUVs) in clinical practice and assessing response to therapy. *Semin Ultrasound CT MR.* 2010;31(6):496–505.
39. Sengoz T, Karakaya YA, Gültekin A, Yaylali O, Senol H, Yuksel D. Relationships of 18F-FDG uptake by primary tumors with prognostic factors and molecular subtype in ductal breast cancer. *Rev Espan Med Nucl Imagen Mol.* 2021;p. S2253–654X(20)30211–0.
40. Hirakata T, Fujii T, Kurozumi S, Katayama A, Honda C, Yanai K, et al. FDG uptake reflects breast cancer immunological features: the PD-L1 expression and degree of TILs in primary breast cancer. *Breast Cancer Res Treat.* 2020;181(2):331–8.
41. Park S, Min EK, Bae SJ, Cha C, Kim D, Lee J, et al. Relationship of the standard uptake value of 18F-FDG-PET-CT with tumor-infiltrating lymphocytes in breast tumors measuring ≥ 1 cm. *Sci Rep.* 2021;11(1):12046.
42. Tian M, He X, Jin C, He X, Wu S, Zhou R, et al. Transpathology: molecular imaging-based pathology. *Eur J Nucl Med Mol Imag.* 2021;48(8):2338–50.
43. Taqi SA, Sami SA, Sami LB, Zaki SA. A review of artifacts in histopathology. *J Oral Maxillofac Pathol JOMFP.* 2018;22(2):279.

Publisher's Note

Springer Nature remains neutral with regard to jurisdictional claims in published maps and institutional affiliations.